

Evolution of broad-line emission from active galactic nuclei

Moshe Elitzur,¹★ Luis C. Ho^{2,3} and Jonathan R. Trump^{4,5}†

¹Department of Physics and Astronomy, University of Kentucky, Lexington, KY 40506-0055, USA

²Kavli Institute for Astronomy and Astrophysics, Peking University, Beijing 100871, China

³The Observatories of the Carnegie Institution for Science, 813 Santa Barbara Street, Pasadena, CA 91101, USA

⁴University of California Observatories/Lick Observatory, University of California, Santa Cruz, CA 95064, USA

⁵Department of Astronomy and Astrophysics, Pennsylvania State University, University Park, PA 16802, USA

Accepted 2013 December 16. Received 2013 November 21; in original form 2013 October 1

ABSTRACT

Apart from viewing-dependent obscuration, intrinsic broad-line emission from active galactic nuclei (AGN) follows an evolutionary sequence: type 1 \rightarrow 1.2/1.5 \rightarrow 1.8/1.9 \rightarrow 2 as the accretion rate on to the central black hole is decreasing. This spectral evolution is controlled, at least in part, by the parameter $L_{\text{bol}}/M^{2/3}$, where L_{bol} is the AGN bolometric luminosity and M is the black hole mass. Both this dependence and the double-peaked profiles that emerge along the sequence arise naturally in the disc-wind scenario for the AGN broad-line region.

Key words: galaxies: active – galaxies: nuclei – quasars: emission lines – quasars: general.

1 INTRODUCTION

Supermassive black holes are ubiquitous in present-day galaxies (Kormendy & Ho 2013). Numerous observations find tight correlations between properties of the host galaxy and its central black hole (Ferrarese & Merritt 2000; Gebhardt et al. 2000; Tremaine et al. 2002; Marconi & Hunt 2003; Greene, Ho & Ulvestad 2006), indicating that the two strongly affect each other's structure and evolution. Understanding this link requires studies of the evolution of supermassive black holes and their immediate environments. Accretion on to the black hole produces observable nuclear activity that may occur in all massive galaxies with a duty cycle of $\sim 10^{-2}$ (Soltan 1982; Marconi et al. 2004; Greene & Ho 2007), and the active galactic nucleus (AGN) bolometric luminosity L_{bol} is directly related to the accretion rate. Since low-luminosity AGN are not simply scaled-down versions of their more familiar cousins (Ho 2008), the classical Seyfert galaxies and quasars, studying the variation with L_{bol} of various AGN radiative signatures sheds light on the evolution of the black hole environment as its accretion rate is decreasing.

Prominent signatures of the pc and sub-pc scales around the black hole include spectral lines from the broad-line region (BLR) and infrared emission from the dusty torus. Observations show that the two are just the inner and outer regions, respectively, of a single, continuous distribution of clouds whose composition undergoes a change at the dust sublimation radius (Elitzur 2008, and references therein). Such a structure arises naturally in the disc-wind scenario, which involves the outflow of clouds embedded in a

hydromagnetic disc wind (Emmering, Blandford & Shlosman 1992; Königl & Kartje 1994; Kartje & Königl 1996; Böttorff et al. 1997; Böttorff, Korista & Shlosman 2000; Everett 2005). Outflows are a common component of AGN (see Everett 2007; Proga 2007, and references therein) and a number of individual sources provide direct observational evidence for the disc-wind structure. Hall et al. (2003) find that only a disc-wind outflow can explain the segregation of broad absorption lines in the BAL quasi-stellar object (QSO) SDSS J0300+0048. From detailed line profile variability studies, Kollatschny (2003) finds evidence for an accretion disc wind in the BLR of the narrow-line Seyfert 1 Mrk 110. Analysis of line dispersion of variable broad-line emission leads to a similar conclusion also for NGC 5548 (Kollatschny & Zetzl 2013), the well-studied AGN whose BLR was successfully modelled in great detail with a clumpy disc outflow by Böttorff et al. (1997). Disc winds also provide satisfactory explanations for the trends exhibited by high-ionization, broad emission lines from 30 000 Sloan Digital Sky Survey (SDSS) quasars (Richards et al. 2011) as well as the general properties of ultraviolet (UV) and X-ray absorption lines in both quasars and Seyfert galaxies (Schurch, Done & Proga 2009; Fukumura et al. 2010). All in all, magnetically driven winds seem to be the best candidate for the origin of high-velocity winds emanating from the inner radii of AGN accretion discs (Peterson 2006; Slone & Netzer 2012).

An immediate consequence of the disc-wind scenario is the prediction that the torus and the BLR disappear at low bolometric luminosities, i.e. low accretion rates (Elitzur & Shlosman 2006). The reason is that, as the mass accretion rate decreases, the mass outflow rate of a disc wind with fixed radial column cannot be sustained below a certain accretion limit. This conclusion, a direct consequence of mass conservation, has been verified in observations. Torus disappearance has been verified in low-luminosity AGN by infrared

★ E-mail: moshe@pa.uky.edu

† Hubble fellow.

observations (van der Wolk et al. 2010; Trump et al. 2011), and the existence of ‘true type 2’ AGN – unobscured sources that lack broad-line emission – has been established in studies by Tran (2001, 2003), Panessa & Bassani (2002) and Laor (2003), among others. In particular, Elitzur & Ho (2009) find that the BLR disappears when $L_{\text{bol}} \lesssim 5 \times 10^{39} M_7^{2/3} \text{ erg s}^{-1}$, where $M_7 = M/10^7 M_\odot$. Note that these ‘true type 2’ AGN differ from the ‘obscured type 2’ class in the historical AGN unified model (Antonucci 1993). While all type 2 AGN have similar optical spectra with narrow emission lines, the ‘true type 2’ AGN intrinsically lack broad emission lines due to structural changes rather than torus obscuration. In this work we use ‘type 2’ to refer to these unobscured ‘true type 2’ AGN.

In a significant recent development, Stern & Laor (2012a,b) studied in detail an SDSS-selected sample of type 1 AGN and found that at low luminosity, most of them actually appear as intermediate types. These observations show that as the accretion rate decreases, the intrinsic AGN classification (apart from torus obscuration) evolves from type 1 to an intermediate type, and finally at low luminosity, potentially to pure type 2. Stern & Laor note that the observational evidence for true type 2 AGN for some previously claimed sources is not yet fully established on the basis of current limits on the absence of broad $H\alpha$ emission. We agree with their assessment. For example, the upper limits to the broad $H\alpha$ luminosity for the majority of the type 2 sources in the Palomar survey (Ho, Filippenko & Sargent 1997, 2003) are not inconsistent with the level of detected X-ray emission (Ho 2009). But this just implies ambiguity, not invalidation, since it does not mean that broad $H\alpha$ must be there; the data are simply not conclusive in demonstrating the complete absence of broad $H\alpha$. Nevertheless, Stern & Laor also noted that there are sources where the absence of broad $H\alpha$ emission is established with such stringent upper limits, well below the level expected from their X-rays, that they indeed appear to be true type 2 AGN. This is qualitatively consistent with the detection of variable nuclear ultraviolet emission in type 2 low-ionization nuclear emission regions (LINERs; Maoz et al. 2005) and X-ray cores with low levels of intrinsic absorption (Ho 2008, and references therein).

Here we advance the view that changes in the accretion rate are responsible for the observed relative strengths of broad emission lines in AGN. We analyse all the available data, including the Stern & Laor sample, in Section 2 and find evidence for a consistent trend of intrinsic BLR evolution with luminosity. In Section 3 we show that the disc outflow scenario offers a natural explanation for the observed spectral evolutionary sequence, and conclude in Section 4 with summary and discussion.

2 INTERMEDIATE-TYPE AGN

Intermediate-type AGN are objects that show broad-line emission at a lower level relative to the narrow lines than in ordinary type 1 sources. The intermediate classification 1.x was originally based on the flux ratio $[O\text{ III}] \lambda 5007/H\beta_{\text{total}}$, which increases from type 1.2 to 1.8; in type 1.9 AGN $H\alpha$ is the only broad emission line seen, possibly reflecting insufficient observational sensitivity (Osterbrock 1981). High-resolution optical or ultraviolet images often reveal the presence of a central point source in intermediates, although the detection difficulty varies depending on the object, the amount of host galaxy dilution and, importantly, the image resolution (Ho 2008). The vast majority also contain X-ray cores with little evidence for intrinsic absorption.

Historical unification posits that in type 1 AGN we have a direct view of the BLR and in type 2 the BLR is obscured (Antonucci 1993). A simple interpolation might suggest that in intermediates

the BLR is either partially obscured or undergoes extinction by optically thin dust, but this contradicts the presence of a visible central point source and the Trippe et al. (2010) finding that the majority of intermediates in their sample are inconsistent with either reddening of the BLR or viewing along a line of sight that grazes the atmosphere of a central dusty torus. Stern & Laor (2012b) find that at low luminosity most type 1 AGN appear as intermediate types, and this cannot be explained by partial obscuration or extinction. These findings show instead that as the accretion rate decreases, broad-line emission progressively declines from its high intensity in quasars and Seyfert 1s to the lower relative strength of intermediate-type AGN, disappearing altogether at sufficiently low luminosities.

2.1 Data analysis

To study this suggested evolution, in Fig. 1 we plot the data assembled in Elitzur & Ho (2009, hereafter EH09) in the $L_{\text{bol}}-M$ plane and its equivalent in the $L_{\text{bol}}-L_{\text{bol}}/L_{\text{Edd}}$ plane, where L_{Edd} is the Eddington luminosity. We exclude from the sample NGC 1068 and NGC 4388, which were formally classified as S1.8 and S1.9 by Ho et al. (1997), respectively, due to the presence of weak broad $H\alpha$ emission, although this is scattered radiation from their well-known hidden type 1 nucleus (Antonucci & Miller 1985; Young et al. 1996). We return to this point below (see Section 4.1). Included are the 8497 high-luminosity sources from Greene & Ho (2007, hereafter GH07) marked as ‘QSO’. Except for the specific designation of intermediate-type sources, the figure is a repeat of the one in EH09 where all broad-line emitters were shown under the single banner of ‘type 1’. To increase the statistical significance for intermediate types we have grouped type 1.2 together with 1.5, and 1.8 with 1.9. For types 1–1.5 the figure additionally includes 48 sources from Winter et al. (2012, hereafter W12). This sample was selected from the all-sky survey conducted with the *Swift* Burst Alert Telescope (BAT) in hard X-rays and thus is largely unbiased towards both obscuration and host galaxy properties. Finally, the figure includes also the sample of unobscured AGN drawn from the Cosmic Evolution Survey (COSMOS; Scoville et al. 2007) by Trump et al. (2011). Of these sources, the 82 marked as ‘BL’ show the broad-line emission typical of type 1 AGN. Meanwhile the 24 marked as ‘NL’ were presumed to be type 2 objects by Trump et al. (2011), based on the absence of broad $H\beta$ line in their spectra. However, the brighter and longer wavelength $H\alpha$ line, needed for confirming this assignment, falls outside the observed spectral range of the ‘NL’ sources, such that they are just as likely to be intermediate-type AGN misclassified only by their limited spectral range.

In spite of some possible mixing of type 1.x and type 2 AGN, the figure reveals an overall segregation between spectral classes of broad-line emitters. Moreover, these classes appear to be stratified roughly in line with the EH09 boundary of broad-line emission, which is reproduced in the figure. To test the possible role of $L_{\text{bol}}/M^{2/3}$ in AGN evolution, Fig. 2 shows the histograms of this variable for the different broad-line spectral classes; histograms using the equivalent Eddington ratio are redundant because they would involve the variable $L_{\text{bol}}(L_{\text{bol}}/L_{\text{Edd}})^2 \propto (L_{\text{bol}}/M^{2/3})^3$. The QSO sample from GH07, shown in the top panel, is sufficiently large to outline a meaningful distribution, faithfully traced by a Gaussian plotted in blue with the sample mean and variance. The BL sources from Trump et al. (2011) have a similar distribution, drawn in red, although their histogram is slightly asymmetric with a higher mean due to the higher luminosity limit of the parent (high-redshift) survey. In contrast, the histogram of type 1 sources

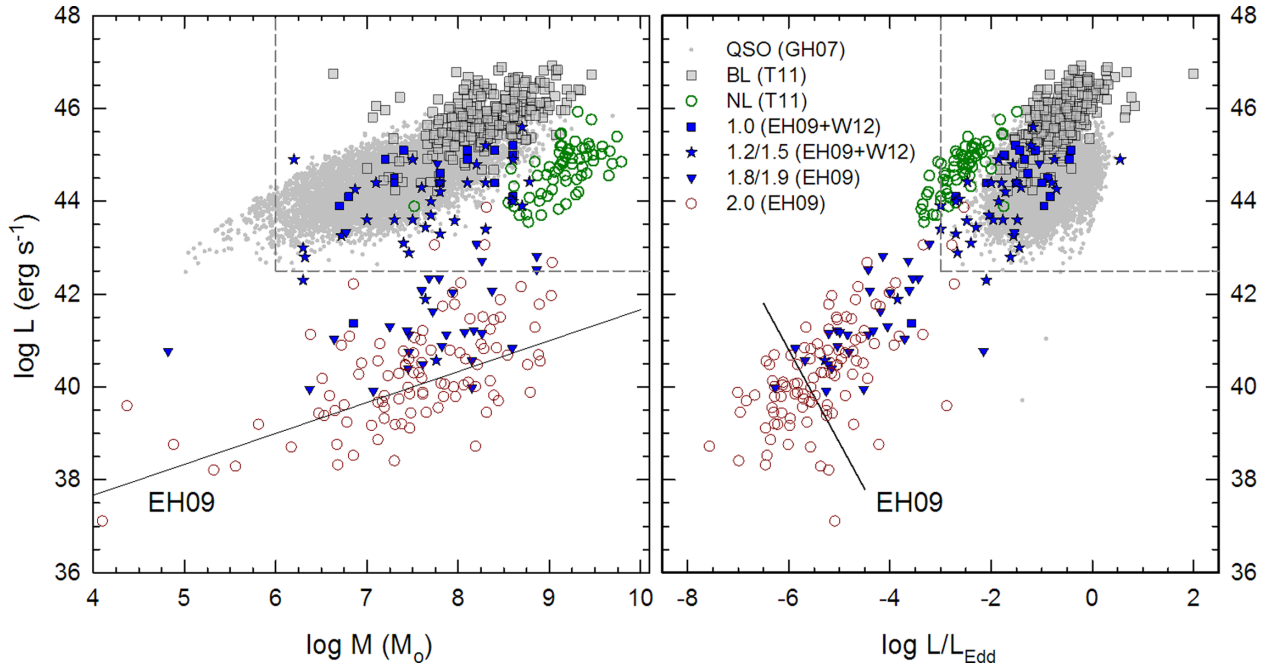


Figure 1. Distribution of black hole masses M (left-hand panels) and Eddington ratios $L_{\text{bol}}/L_{\text{Edd}}$ (right-hand panels) versus bolometric luminosity L_{bol} for objects separated by spectral classification. Objects marked as ‘QSO’ refer to the sample of quasars and high-luminosity Seyfert 1 nuclei studied by Greene & Ho (2007, GH07). The ‘BL’ and ‘NL’ labels are for sources from the COSMOS survey classified as, respectively, broad- and narrow-line emitters by Trump et al. (2011, T11). Objects marked by the numerical classification of their AGN type are from Elitzur & Ho (2009, EH09) and Winter et al. (2012, W12). The solid lines labelled EH09 show the bounds on broad-line emission found in Elitzur & Ho (2009, EH09): (left) $\log L = 35 + \frac{2}{3} \log M$ and (right) $\log L = 28.8 - 2 \log(L/L_{\text{Edd}})$. Dashed grey lines delineate the domains of the Stern & Laor (2012a,b) sample, analysed separately in Section 2.2.

from W12, drawn in green, has essentially the same mean and, accounting for the smaller sample size, shape as the QSO sample. Thus, the low-redshift W12 compilation has a similar luminosity limit as the GH07 sample. With the uncertainties surrounding their spectral classification, the NL sources from Trump et al. (2011) are shown in the middle panel together with the combined sample of type 1.2/1.5 sources from W12 and EH09. The two distributions are similar, both in shape and mean m , giving support to the conjecture that the NL sources might be actually intermediate-type rather than type 2 AGN.

Further statistical analysis for each spectral class is not warranted because of the small sample sizes for all but the GH07 data set (notice the large disparity between the histogram counts). Still, Fig. 2 establishes an unmistakable trend: when $L_{\text{bol}}/M^{2/3}$ is decreasing, AGN broad-line emission evolves away from type 1 towards higher values of the intermediate sequence, disappearing altogether below the EH09 limit where all AGN become ‘true type 2’.

2.2 The Stern & Laor sample

Stern & Laor (2012a) have recently studied an SDSS-selected sample of 3410 type 1 AGN. Dashed grey lines in Fig. 1 outline the regions of parameter space where these sources fall. Although this sample (hereafter SL12) does not extend to luminosities lower than $10^{42} \text{ erg s}^{-1}$ and Eddington ratios below 10^{-3} , Stern & Laor (2012b) were still able to discern the transition to intermediate spectral classes at decreasing luminosities. From a careful decomposition of the $\text{H}\alpha$ profile into broad and narrow components, with respective luminosities $L_{\text{bH}\alpha}$ and $L_{\text{nH}\alpha}$, they show that the narrow component starts dominating the total $\text{H}\alpha$ profile when the luminosity decreases, and that at $L_{\text{bH}\alpha} \lesssim 10^{42} \text{ erg s}^{-1}$ intermediate-type AGN dominate the population of broad-line emitters: at $L_{\text{bH}\alpha} \gtrsim$

$10^{43} \text{ erg s}^{-1}$ the mean $\text{H}\alpha$ profiles are typical of Seyfert 1.0s, at $L_{\text{bH}\alpha} \sim 10^{42} \text{ erg s}^{-1}$ they are typical of Seyfert 1.5, while at $L_{\text{bH}\alpha} \sim 10^{40} - 10^{41} \text{ erg s}^{-1}$, broad-line objects tend to be Seyfert 1.8s. Stern & Laor also show that Seyfert 1.5 and 1.8 can be defined analytically using the $L_{\text{nH}\alpha}/L_{\text{bH}\alpha}$ ratio, with $L_{\text{nH}\alpha}/L_{\text{bH}\alpha} \approx 0.1$ marking the transition from type 1.0 to 1.5 and $L_{\text{nH}\alpha}/L_{\text{bH}\alpha} \approx 0.3$ the transition to 1.8.

Dr J. Stern has kindly provided us the data for the full SL12 sample (table 1 in Stern & Laor 2012b). We have classified the sources according to the Stern & Laor $L_{\text{nH}\alpha}/L_{\text{bH}\alpha}$ criteria and found 1266 type 1.0 objects, 1306 type 1.5, and 838 type 1.8. Fig. 3 shows the $L_{\text{bol}}-M$ and $L_{\text{bol}}-L/L_{\text{Edd}}$ distributions for this sample, the analog of Fig. 1. Because of the high density of points, this sample is shown with contour plots instead of a scatter diagram. Although limited to relatively luminous objects, the SL12 sample still shows the same stratification by spectral class as in Fig. 1 and the same sequence in terms of the variable $L_{\text{bol}}/M^{2/3}$. These trends stand out more prominently in Fig. 4, which shows histograms binned in $L_{\text{bol}}/M^{2/3}$ for the three spectral classes, displaying a behaviour similar to that seen in Fig. 2. The mean for type 1.0 sources is essentially the same as for the GH07 and W12 samples. For the intermediates, the mean values are higher for the SL12 sample because the entire low-luminosity end is missing. Still, the SL12 sample captures the trend of decreasing $L_{\text{bol}}/M^{2/3}$ along the spectral sequence $1.0 \rightarrow 1.5 \rightarrow 1.8$ thanks to its large size. To assess the validity of the differences between the mean values of $L_{\text{bol}}/M^{2/3}$ we ran two statistical tests for the null hypothesis that there are no inherent differences between the objects in the three classes (i.e. all are drawn from the same underlying population). The two-sample Kolmogorov–Smirnov (KS) test for the 1.0 and 1.5 classes returned a D -statistic of 0.25, for a probability $p = 9 \times 10^{-37}$ of being wrong in concluding that there is a true difference in the two groups. The corresponding values

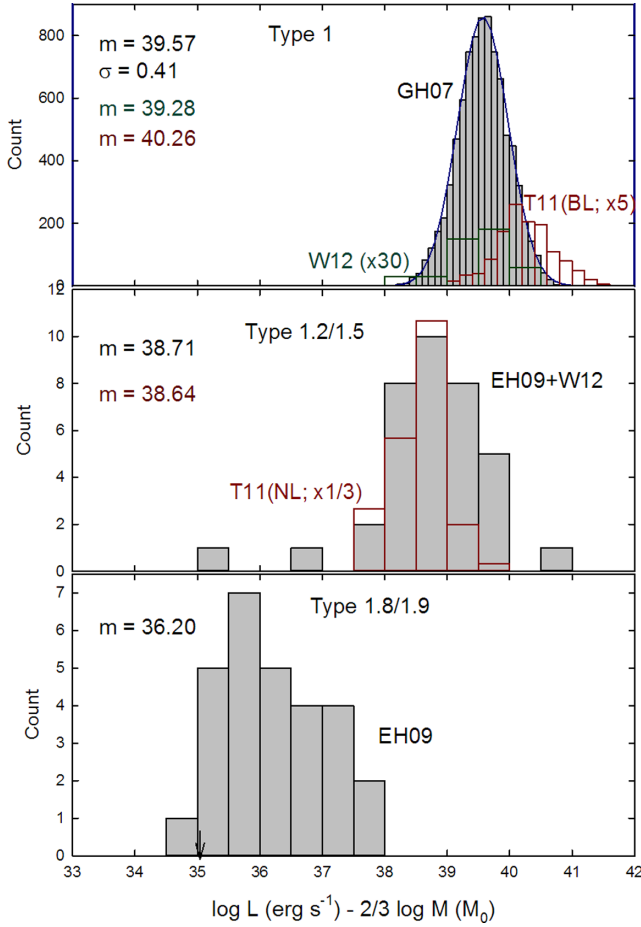


Figure 2. Histograms of different classes of broad-line AGN binned by $L_{\text{bol}}/M^2/3$. The distribution mean, m , is listed in each panel and the arrow on the bottom axis marks the location of the EH09 bound shown in Fig. 1. References for the data are listed in Fig. 1. The top panel shows the histogram of the type 1 sources from GH07 and lists its standard deviation σ in addition to the mean. A Gaussian plot with the listed values of m and σ is shown in a blue line. The histograms of type 1 sources from W12 (multiplied by factor of 30 for clarity and drawn in green) and the BL sources from T11 (multiplied by factor of 5, in red) are plotted separately. The T11 sample NL sources histogram (in red, divided by 3) is shown in the middle panel together with the type 1.2/1.5 histogram from EH09 and W12.

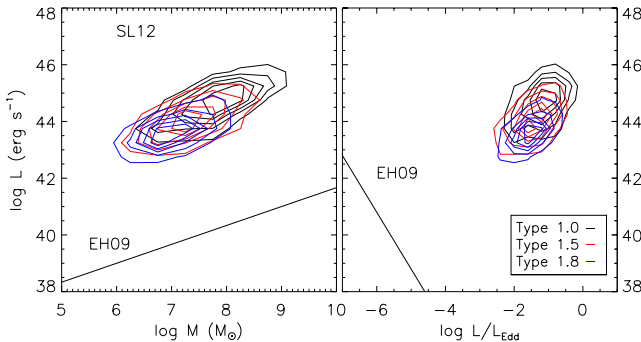


Figure 3. Analog of Fig. 1 for the Stern & Laor (2012a,b) sample (SL12). Because of the high density of points, the source distribution of each AGN type is shown by coloured contours evenly spaced in point density at 83, 67, 50, 33 and 17 per cent of the maximum. The EH09 boundaries are drawn for guidance. Echoing Fig. 1, there are significant changes in the mean AGN properties from type 1.0 to 1.5 to 1.8.

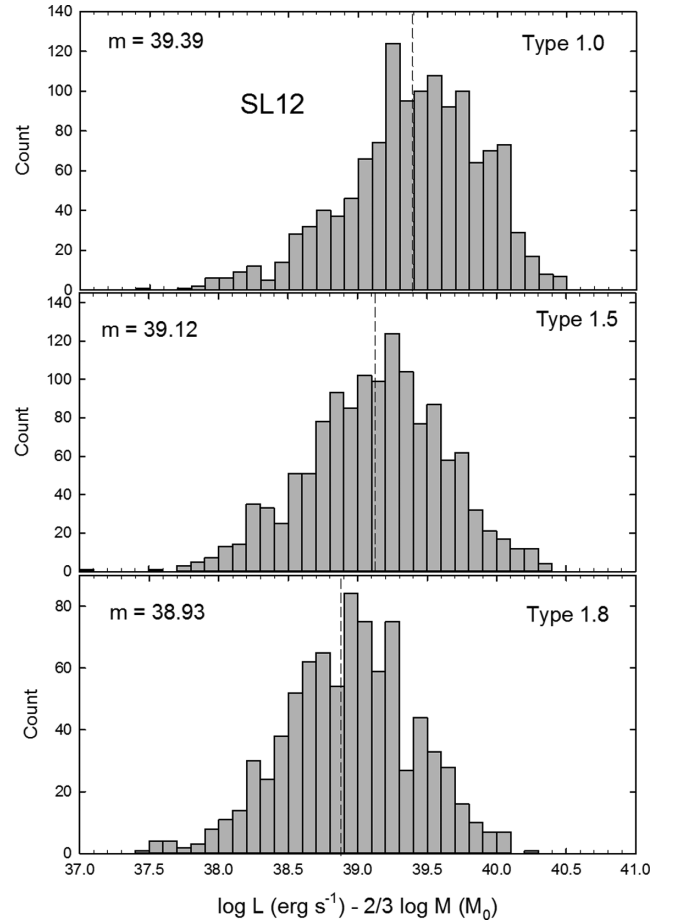


Figure 4. Histograms for spectral classes of the SL12 sample, binned by $L_{\text{bol}}/M^2/3$. In each panel, the distribution mean m is listed and drawn as a vertical dashed line.

for the comparison between the 1.5 and 1.8 classes were $D = 0.33$ and $p = 7 \times 10^{-62}$. Another widely used method is the Mann–Whitney (MW; Mann & Whitney 1947) rank sum test. For sample sizes n_1 and n_2 , the MW U -statistic returns values between 0 (no overlap between the samples) and $0.5n_1n_2$. For the 1.0–1.5 comparison, the MW test returned $U = 0.34n_1n_2$ for $p(\text{MW}) = 1 \times 10^{-42}$, for the 1.5–1.8 comparison the results were $U = 0.39n_1n_2$ and $p(\text{MW}) = 5 \times 10^{-19}$. Both tests show with overwhelming probabilities that the differences between the mean values of $L_{\text{bol}}/M^2/3$ for the three spectral classes are real.

Stern & Laor (2012b) suggest that the transition to intermediate types at decreasing luminosity reflects an increase in the relative strength of the $H\alpha$ narrow component rather than a decrease of the broad component emission. This suggestion was based on their conclusion that $L_{\text{bH}\alpha}$ is proportional to the AGN bolometric luminosity, i.e. the broad component ‘covering factor’ $L_{\text{bH}\alpha}/L_{\text{bol}}$ is the same for all broad-line sources, independent of luminosity. The evidence came from fig. 10 in Stern & Laor (2012a), which displays tight correlations between $L_{\text{bH}\alpha}$ and the AGN monochromatic luminosity νL_ν in various spectral bands, from 2 keV all the way to 2.2 μm . In particular, the tightest proportionality is shown by the 2 keV X-rays (top left-hand panel in fig. 10 of Stern & Laor 2012a), the spectral region least contaminated by contributions from star formation. We reproduce this correlation in Fig. 5, only instead of $L_{\text{bH}\alpha}$ we plot the ratio $L_{\text{bH}\alpha}/L_X$, a proxy for the broad component covering factor, versus L_X , which is generally regarded the most reliable indicator

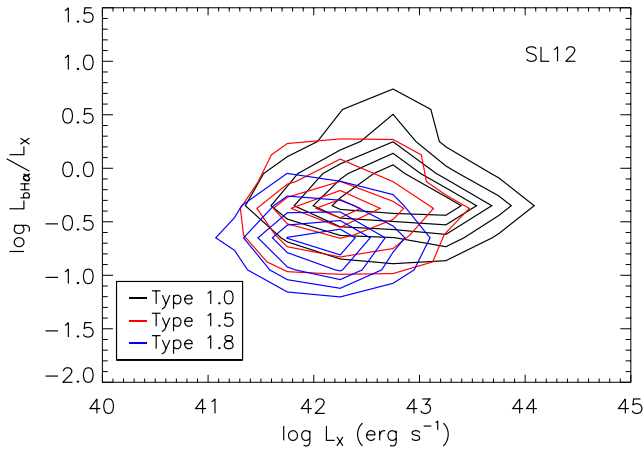


Figure 5. Contours (as in Fig. 3) for the SL12 sample of the ratio of broad-line and 2 keV X-ray luminosities, equivalent to broad-line covering factor, versus X-ray luminosity, a proxy for the bolometric luminosity. The mean broad-line ‘covering fraction’ decreases along the sequence from type 1.0 to 1.5 to 1.8.

of AGN bolometric luminosity. Importantly, instead of a scatter diagram with all sources marked by the same symbol as done in Stern & Laor (2012a) we distinguish between the spectral classes using different colour contour plots. The figure shows a clear trend of covering factor variation among the different spectral classes. Because of the large scatter (more than two orders of magnitude) of the sample data, lumping all the sources together in a single scatter diagram masked this trend in the Stern & Laor analysis.

To tease out this effect more clearly, Fig. 6 shows histograms of the effective covering factors $L_{bH\alpha}/L_X$ and $L_{nH\alpha}/L_X$ for the H α broad and narrow components, respectively, for the SL12 sample. The right-hand column of panels show that, as suggested by Stern & Laor, the narrow component covering factor indeed increases along the 1.0→1.5→1.8 sequence. This increase likely arises from the increased prominence of the star formation contribution to H α emission relative to the AGN when the latter’s luminosity is decreasing. As such, this effect reflects external conditions, not any intrinsic variation in the AGN structure. Meanwhile the left-hand column of Fig. 6 shows that, together with the increase in the narrow component covering factor, the broad component covering factor is *decreasing* along the 1.0→1.5→1.8 sequence. To assess the validity of this effect we again ran statistical tests for the null hypothesis that there are no meaningful differences between the broad H α effective covering factors of the three classes. For the 1.0–1.5 comparison the KS test returned $D(KS) = 0.17$ for $p(KS) = 1 \times 10^{-12}$, and the MW test produced $U(MW) = 0.36n_1n_2$ and $p(MW) = 1 \times 10^{-33}$. For the 1.5–1.8 comparison the corresponding results were $D(KS) = 0.23$ for $p(KS) = 6 \times 10^{-20}$, and $U(MW) = 0.35n_1n_2$ for $p(MW) = 4 \times 10^{-32}$. Both tests decisively show that the differences between the classes are real. They are also highly significant: the difference in $\log(L_{bH\alpha}/L_X)$ of 0.37 dex implies that the broad component covering factor of type 1.8 AGN is, on average, less than half that in type 1.0.

We have attempted to verify that $L_{bH\alpha}/L_X$ declines even further at lower luminosities but only met with partial success for lack of sufficient data. The EH09 sample contains 29 sources of type 1.8/1.9 and only 10 of type 1.2/1.5. An additional 26 type 1.2/1.5 sources from the W12 sample have greatly aided the analysis in Section 2.1, especially the histograms shown in Fig. 2. Unfortunately, the W12 sample has not yet been subjected to detailed spectral analysis to

decompose the H α line to its broad and narrow components, and thus could not be used for studying covering factors. Faced with the inadequate number of 1.2/1.5 objects in the EH09 sample, we decided to lump them together with the 1.8/1.9 sources for an overall set of 39 low-luminosity intermediate-type sources. All necessary data for these objects are tabulated in Ho et al. (1997) and Ho (2009), including X-ray luminosity integrated over 2–10 keV, which we converted to the Stern & Laor 2-keV L_X assuming an X-ray slope of $\Gamma = 1.9$ over this range.

The results are shown in Fig. 6, where the EH09 histograms are plotted in the bottom panels because the sample is dominated by 1.8/1.9 sources. The ratio $L_{bH\alpha}/L_X$ decreases further from its value for the higher luminosity 1.8 AGN of the SL12 sample, as expected from a quantity reflecting intrinsic AGN variation. The decrease in mean values between 1.8/1.9 sources in the SL12 and EH09 samples is about a factor of 70 in luminosity, a factor of 440 in $L_{bol}/M^{2/3}$ and a factor of 5 in the effective broad-line covering factor $L_{bH\alpha}/L_X$. Because of the small number statistics at the low-luminosity end this result cannot be taken too literally, but the underlying effect is clearly established – the ratio $L_{bH\alpha}/L_X$ decreases continuously and significantly with $L_{bol}/M^{2/3}$. In contrast, the variation of the ratio $L_{nH\alpha}/L_X$ between the two data sets is entirely out of line with the luminosity trend within the SL12 sample. Remarkably, the average value of $\log L_{nH\alpha}/L_X$ for the EH09 sample (−1.58) is indistinguishable from that for the SL12 type 1.0 objects, whose narrow H α emission is presumably least complicated by host galaxy contamination. This reflects the fact that the Palomar spectra for the EH09 objects – all nearby systems – properly isolate the emission from the galaxy nuclei (Ho et al. 1997). The $L_{nH\alpha}/L_X$ values for the EH09 sample should not be significantly contaminated by host galaxy emission.

The systematic change of $L_{bH\alpha}/L_X$ with AGN type seen in the left-hand panel of Fig. 6 is not due to variations of L_{bol}/L_X with luminosity. While the X-ray bolometric correction does change with decreasing luminosity, the variation is too small to account for the observed trend. Over the entire 2–10 keV luminosity range of 10^{42} – 10^{45} erg s $^{-1}$ covered by the Stern & Laor sample, $L_{bol} \approx 45L_{2-10\text{keV}}$ within ± 5 per cent (Runnoe, Brotherton & Shang 2012), while the mean value of the ratio $L_{bH\alpha}/L_X$ decreases by more than a factor of 2 between type 1.0 and 1.8 sources. And for the extreme luminosities of the EH09 sample, which span $L_{2-10\text{keV}} \approx 10^{38}$ – 10^{42} erg s $^{-1}$, the X-ray bolometric correction changes only by a factor of ~ 3 , to $L_{bol} \approx 16L_{2-10\text{keV}}$ (Ho 2008), yet the mean value of $L_{bH\alpha}/L_X$ is down by a factor of 12 from that of the 1.0 sources.

As an additional check of the veracity of this result we have repeated the analysis substituting UV (1528 Å monochromatic luminosity) for the X-rays. Not all of the SL12 sources have UV data, reducing slightly the sample sizes for 1.0, 1.5 and 1.8 classes to 1119, 1165 and 736, respectively. The results are shown in Fig. 7, presenting the same data as fig. 7 of Stern & Laor (2012b) but in a separate histogram for each class instead of a single scatter diagram for all sources. The similarity with the trend seen in Fig. 6 is evident and the statistical tests confirm what is discernible to the eye. Comparing the 1.0 and 1.5 classes, the KS test returns $D(KS) = 0.10$ for a probability $p(KS) = 2 \times 10^{-5}$ of being wrong in concluding that the two are different. On the other hand, the MW test produces $U(MW) = 0.49n_1n_2$ and $p(MW) = 0.47$; this test cannot exclude the possibility that the difference between the two sets is due to random sampling variability. The MW test is inconclusive because it is mostly sensitive to differences between the sample medians, which are the same (−1.60) for both. In contrast, the KS test is decisive because it compares the distribution shapes, and these are

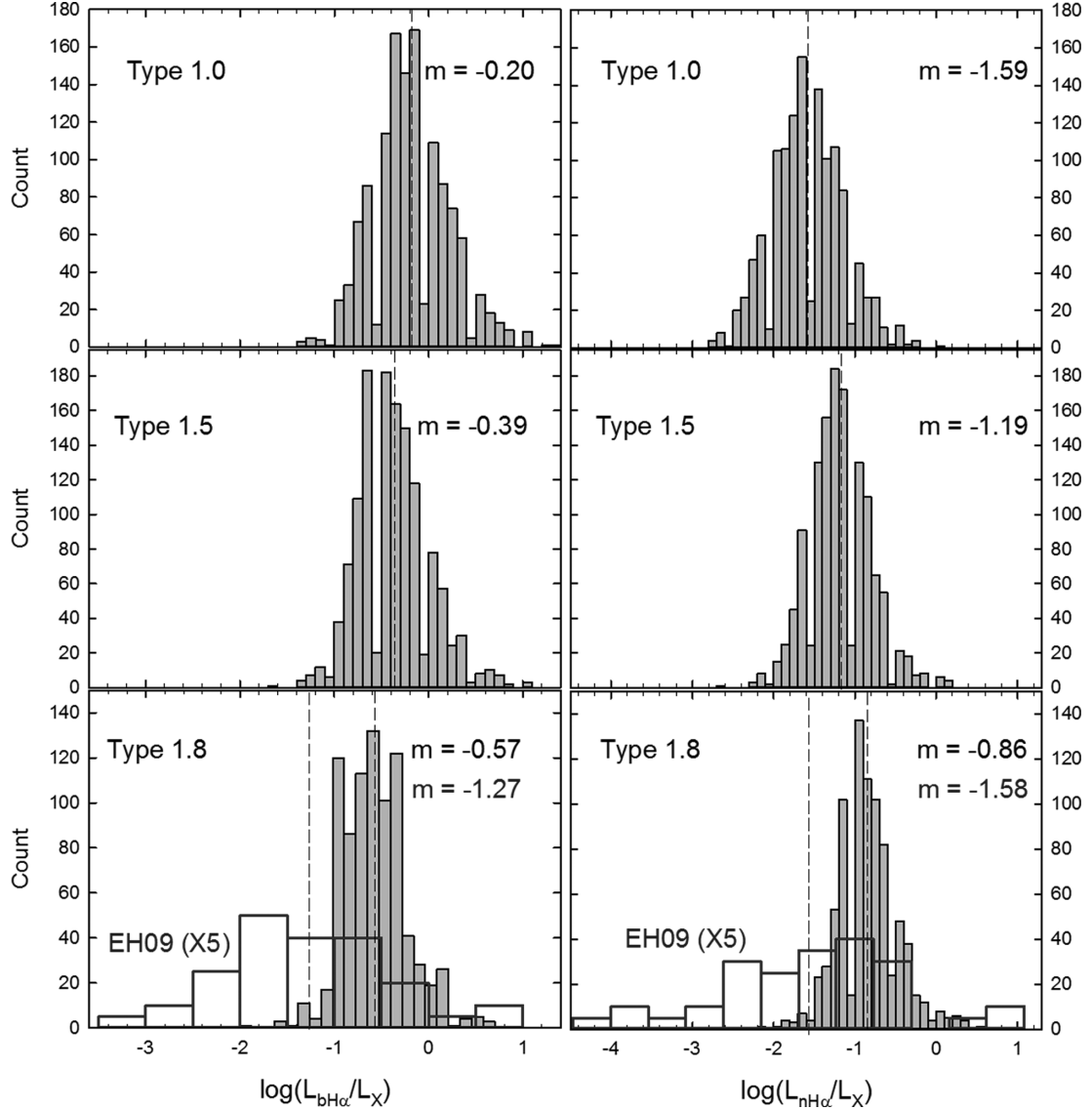


Figure 6. ‘Covering factor’ histograms of the H α broad (left) and narrow (right) components for the SL12 sample. The spectral class is marked in each panel and the mean value of the logarithm of ‘covering factor’ is listed and drawn as a vertical dashed line. The lower panels show also (in red) the histograms for all the intermediate-type sources in the EH09 sample; see text for details. Note the great similarity between the mean values of $L_{\text{bH}\alpha}/L_X$ of the EH09 sources and the SL12 type 1.0s.

significantly different from each other. There are no such ambiguities in the comparison of the 1.5 and 1.8 samples, which yields $D(\text{KS}) = 0.22$ for $p(\text{KS}) = 2 \times 10^{-12}$ and $U(\text{MW}) = 0.35n_1n_2$ for an overwhelming $p(\text{MW}) = 2 \times 10^{-110}$ (the returned U -value is 22σ away from the mean); these are very clearly different types of objects.

Thus the UV data reaffirm the trend established through the X-rays. Denote by L_m the monochromatic luminosity in either X-ray or UV band. Then $L_{\text{bH}\alpha}/L_m = \zeta_m L_{\text{bH}\alpha}/L_{\text{bol}}$, where $\zeta_m = L_{\text{bol}}/L_m$ is the bolometric correction for the corresponding band. Going from high to low luminosities, the bolometric corrections display the opposite behaviour in the two bands – ζ_m is decreasing for X-rays and increasing for UV. Yet both bands display the same trend of variation of $L_{\text{bH}\alpha}/L_m$ with decreasing luminosity over the SL12 sample, showing conclusively that $L_{\text{bH}\alpha}/L_{\text{bol}}$ is decreasing through the spectral class sequence 1.0 \rightarrow 1.5 \rightarrow 1.8. A potential slight increase in ζ_{UV} throughout the SL12 sample could partly offset the

intrinsic decrease of $L_{\text{bH}\alpha}/L_{\text{bol}}$, bringing the mean values for the 1.0 and 1.5 classes into equality and making the MW test inconclusive, although the KS test remains decisive. Such an increase would still be insufficient to bridge the larger gap to the 1.8 sources, where both tests remain overwhelmingly decisive.

There is no tabulation of UV data for the EH09 sources, so we maintain $L_{\text{bH}\alpha}/L_X$ as our primary indicator for the conversion efficiency of continuum radiation to broad-line emission. Fig. 8 summarizes the results. The data establish, with high significance, that the average effective covering factor $L_{\text{bH}\alpha}/L_X$ decreases with $L_{\text{bol}}/M^{2/3}$ along the 1.0 \rightarrow 1.5 \rightarrow 1.8 sequence, albeit with scatter causing some overlap among the AGN types. As is evident from Fig. 1, the SL12 data set samples only the highest luminosity end of intermediate-type AGN and thus captures only the high-end boundaries of the 1.5 and 1.8 luminosity distributions. But thanks to its sizeable number of sources, the differences it shows between those boundaries are highly significant as verified by independent

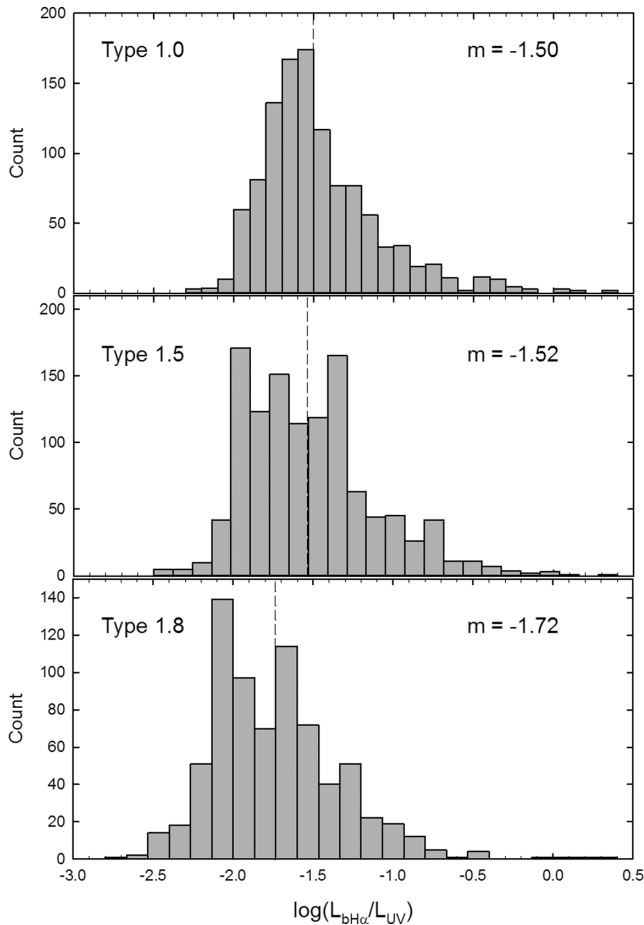


Figure 7. ‘Covering factor’ histograms for the SL12 sample broad H α component similar to Fig. 6, only for UV instead of X-ray luminosity.

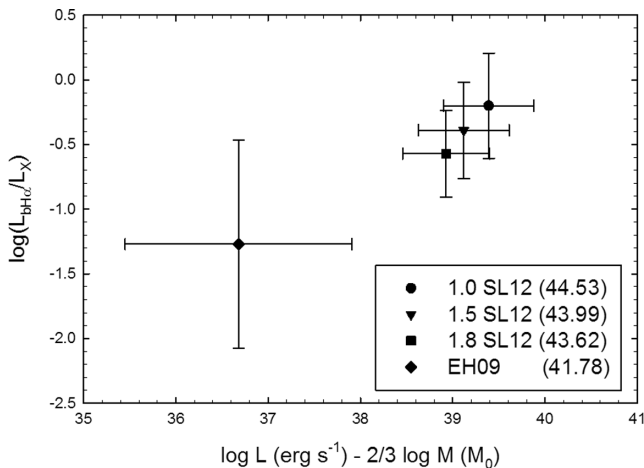


Figure 8. Scatter diagram for the mean of broad H α ‘covering factor’ for the various families of broad-line sources identified by their labels. Error bars indicate one standard deviation. The numbers in parentheses are the means of $\log L_{\text{bol}}$ (erg s $^{-1}$) for each group.

statistical tests. Among the SL12 sources, the covering factor decreases by more than a factor of 2 from type 1.0 to 1.8. The EH09 sample shows that the decrease continues further at lower luminosities, its mean value of $L_{\text{bH}\alpha}/L_X$ is a factor of 12 lower than for the type 1.0 sources. Even accounting for a decrease in the X-ray bolometric

metric correction and for the fact that the small size of the EH09 sample implies that its mean value is less well constrained, it seems safe to conclude that, on average, $L_{\text{bH}\alpha}/L_X$ is at least a factor of 3 smaller for type 1.8/1.9 AGN than for type 1.0. Since the immediate vicinity of the central black hole is the only likely source of high-ionization lines with widths in excess of 1000 km s $^{-1}$, the decline of the broad H α covering factor reflects a *significant intrinsic change in the BLR at decreasing luminosities*.

2.3 Double-peaked emission in intermediate types

As shown in the previous section, low-luminosity, low-Eddington ratio systems with broad emission lines are typically of the type 1.8 or 1.9 variety. Another notable property of intermediate types involves double-peaked broad-line profiles, attributed to emission from rotating discs. Such profiles are found in only about 3 per cent of the general broad-line AGN population (Strateva et al. 2003) and most double-peak emitters have accretion rates considerably lower than the Eddington limit (Eracleous & Halpern 2003; Eracleous, Lewis & Flohic 2009). Conversely, low-luminosity, low-Eddington ratio systems have a fairly high detection rate of double-peaked profiles (Ho et al. 2000; Ho 2008). Significantly, many of the 1.8 and 1.9 AGN show double-peaked broad-line profiles while most types 1.2/1.5 do not. The detection of double-peaked broad H α in low-luminosity AGN is greatly facilitated by small-aperture spectroscopy afforded by the *Hubble Space Telescope* (HST; e.g. Ho et al. 2000; Shields et al. 2000). Unfortunately, a uniform HST spectroscopic census of the EH09 sample is not available, and thus we do not have robust statistics on the incidence of double-peaked broad H α emission in these objects.

3 A TWO-COMPONENT BLR

General considerations of AGN broad-line modelling suggest that the emission originates from a collection of clouds (e.g. Netzer 1990). Significant contributions from the intercloud medium are precluded by its lower density, which implies a higher ionization parameter. Direct observational evidence for the clumpy nature of the BLR comes from studies of X-ray variability (Risaliti, Elvis & Nicastro 2002) and from a detailed study of a set of absorption lines in a quasar outflow (Hall et al. 2007). As shown above, two phenomena stand out along the 1.0 \rightarrow 1.2/1.5 \rightarrow 1.8/1.9 sequence: the fraction of bolometric luminosity converted to H α broad-line emission decreases, and double-peaked profiles, signatures of rotating disc emission, appear. The simultaneous emergence of two such disparate effects can be understood if as the luminosity is decreasing, the BLR cloud distribution is gradually losing the components with the highest elevations above the disc. Cloud motions near the disc surface can be expected to reflect more closely Keplerian velocities, which is why double peaked profiles would emerge in that case. Additionally, lower elevations also reduce the line emission strength because the BLR geometrical covering factor, the fraction of the AGN sky covered by clouds, becomes smaller, intercepting a smaller fraction of the ionizing continuum. On top of that, the UV/optical continuum emission from the AGN accretion disc decreases towards its equatorial plane (Laor & Netzer 1989; Sun & Malkan 1989; Kawaguchi & Mori 2010), an effect that was demonstrated convincingly by Risaliti, Salvati & Marconi (2011) in a recent study of [O III] equivalent widths. The combined effect of a smaller geometrical covering and a decrease in the ionizing continuum

intensity enhances the impact that a reduction in the height of the cloud distribution has on broad-line emission.

Kartje, König & Elitzur (1999) were the first to note that such a structural change in the cloud distribution occurs naturally in the disc-wind scenario at lower luminosities. We now describe this effect.

3.1 Cloud trajectories

Disc outflow models are based on the seminal Blandford & Payne (1982) self-similar solution for a cold hydromagnetic wind driven centrifugally along rotating magnetic field lines anchored in the disc. Rees (1987) pointed out that if such winds were seeded with unmagnetized clouds, a configuration known as ‘melon seed’ plasma, they could offer a solution to the long standing problem of BLR cloud confinement. In that case the clouds move as diamagnetic blobs that can exclude (‘push aside’) the field while being confined by the magnetic pressure of the surrounding plasma. Adopting this approach, Emmering et al. (1992) extended the Blandford & Payne solution to clumpy disc outflows. Accounting for the change in composition across the dust sublimation radius:

$$R_d \simeq 0.4 L_{45}^{1/2} \text{ pc}, \quad (1)$$

where $L_{45} = L_{\text{bol}}/10^{45} \text{ erg s}^{-1}$ (Nenkova et al. 2008), the BLR and torus were unified in a single outflow: at radii beyond R_d the clouds are dusty and comprise the AGN obscuring torus, while the wind regions between R_d and some $R_{\text{in}} < R_d$ contain the broad-line emitting clouds. Emmering et al. showed that modelling the BLR as a clumpy disc outflow yields good agreement with observations (see Section 3.2.2).

Kartje et al. (1999) considered similarly a wind that uplifts by its ram pressure and confines by its magnetic pressure dense clouds fragmented from the disc. Since the focus of their work was on water maser emission, Kartje et al. considered clouds at $r > R_d$ while noting that they differ from BLR clouds only in their composition, which does not affect the dynamics. But whereas Emmering et al. assumed the clouds to move along the outflow streamlines, Kartje et al. dropped this assumption and studied the actual motions of diamagnetic blobs carried by the wind. Even if there were no field in the clouds originally, it would gradually penetrate and breakup the clouds, but this process is expected to be slower than the sound speed within the clouds (Rees 1987). Following Kartje et al. we ignore this effect and consider the motion of ‘melon seed’ clouds confined by the wind magnetic pressure while accelerated by its ram pressure against the gravitational pull of the central black hole. The equation of motion of such a cloud with mass M_c , velocity vector \mathbf{v}_c and cross-sectional area A_c normal to its motion relative to the wind is then

$$\frac{d\mathbf{v}_c}{dt} \approx -\frac{GM}{r^2} \hat{\mathbf{r}} + \frac{\rho_w A_c}{M_c} |\mathbf{v}_w - \mathbf{v}_c| (\mathbf{v}_w - \mathbf{v}_c), \quad (2)$$

where $\hat{\mathbf{r}}$ is unit vector in the radial direction, and \mathbf{v}_w and ρ_w are the wind velocity and mass density, respectively (Kartje et al. 1999). The cloud properties enter only through the column density $N_{\text{H},c} = M_c/(m_{\text{H}} A_c)$, where m_{H} is the proton mass, that characterizes the cloud whatever its geometrical shape. For spherical uniform clouds, $N_{\text{H},c}$ is $\frac{2}{3}$ the column along the diameter. In the case of a thin, extended slab, averaging over orientations yields $N_{\text{H},c}$ that is twice the column along the slab normal.

The wind density ρ_w can be found from its mass outflow rate \dot{M}_w through mass conservation. For the Blandford & Payne solution, $\dot{M}_w = 4\pi r^2 \rho_w v_w \ln(R_d/R_{\text{in}})$. Since the BLR relative thickness is

likely $R_d/R_{\text{in}} \lesssim 100$ (Emmering et al. 1992), the logarithmic factor is probably $\lesssim 4$ and is omitted for simplicity. The only property of the clouds that enters is their column density. This suggests that we convert also \dot{M}_w to an equivalent column density. The ratio $\dot{M}_w/(r v_K)$, where $v_K = (GM/r)^{1/2}$ is the local Keplerian velocity, has dimensions of surface density; thus we introduce

$$N_{\text{crit}} = \frac{\dot{M}_w}{4\pi m_{\text{H}} r v_K} = N_{\text{crit}}(R_d) \left(\frac{R_d}{r} \right)^{1/2}, \quad (3)$$

where the factor 4π is added for convenience. The cloud equation of motion (equation 2) can then be written as

$$\frac{d\mathbf{v}_c}{dt} \approx -\frac{v_K^2}{r} \hat{\mathbf{r}} + \frac{v_K^2}{r} \frac{N_{\text{crit}}}{N_{\text{H},c}} \frac{1}{v_K v_w} |\mathbf{v}_w - \mathbf{v}_c| (\mathbf{v}_w - \mathbf{v}_c). \quad (4)$$

Clouds carried along the wind streamlines have $\mathbf{v}_c \parallel \mathbf{v}_w$. Projecting on the wind direction, the equation of motion for such clouds becomes

$$\frac{dv_c}{dt} \approx \frac{v_K^2}{r} \left[\frac{N_{\text{crit}}}{N_{\text{H},c}} \frac{v_w}{v_K} \left(1 - \frac{v_c}{v_w} \right)^2 - \cos \theta \right], \quad (5)$$

where θ is the angle between the wind velocity and the radial direction. For a cloud to be accelerated along a streamline by the wind ram pressure, the quantity inside the square brackets must be positive.

Consider first the cloud initial motion near the disc surface, then θ is the wind launch angle measured from the disc surface (typically $\sim 20^\circ$ in the Blandford & Payne solution). The magnitude of the wind launch velocity is comparable to the local turbulence velocity in the disc, which is roughly 10 per cent of the local Keplerian velocity (Elitzur & Shlosman 2006); that is, $v_w \ll v_K$ close to the disc (in the Blandford & Payne solution, the launch velocity of the cold wind is taken as 0). Therefore, the term in square brackets in equation (5) can be positive only when $N_{\text{H},c} < N_{\text{crit}}$; clouds must be subcritical to accelerate along the wind streamlines. To ensure that such clouds can follow the rising trajectory shown in Fig. 9 we must verify that their acceleration remains positive away from the

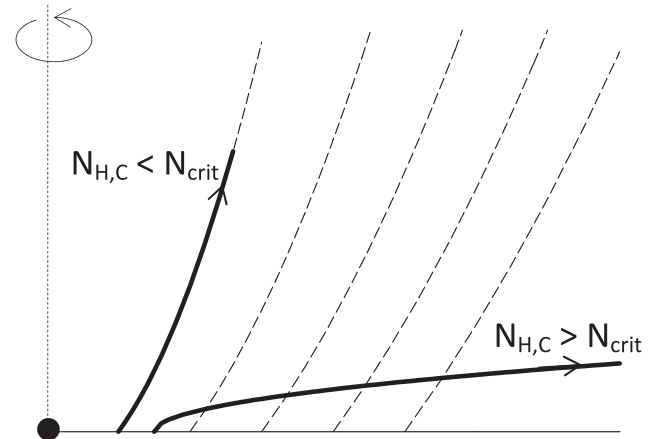


Figure 9. Schematic representation of clumpy outflow from an AGN accretion disc. Dashed lines show wind streamlines projected into the poloidal plane. Trajectories of clouds uplifted by the wind ram pressure, shown by solid heavy lines, depend on their column density $N_{\text{H},c}$. Subcritical clouds, with $N_{\text{H},c} < N_{\text{crit}}$ (equation 3), tend to follow the wind streamlines while supercritical clouds, $N_{\text{H},c} > N_{\text{crit}}$, tend to move across streamlines and remain close to the disc surface, as first noted by Kartje et al. (1999; see their fig. 7).

disc. Indeed, both relevant ratios increase as the cloud rises. The ratio v_w/v_K increases because of the wind acceleration. Confinement by the wind magnetic pressure implies that the gas density inside clouds obeys $n_{H,c} \propto B^2$. With a constant cloud mass and the outflow magnetic field $B \propto r^{-5/4}$ from Blandford & Payne, the radial variation of the cloud properties is $n_{H,c} \propto r^{-5/2}$, $R_c \propto r^{5/6}$ and $N_{H,c} \propto r^{-5/3}$. Therefore the ratio $N_{crit}/N_{H,c}$ increases with distance as $r^{7/6}$ – clouds that start subcritical will remain so. It is also important to note that, in spite of the magnetic pressure confinement, the cloud column density decreases as it rises above the disc. The vertical range of broad-line emission is thus limited, resulting in a toroidal geometry for the BLR.

Supercritical clouds, those with $N_{H,c} > N_{crit}$, cannot float with the wind. Instead, they tend to ‘sink’ and move across the wind streamlines. These clouds remain close to the disc surface, similar to the low-lying cloud trajectory in Fig. 9, with their motions closely mirroring the disc Keplerian velocity field (Kartje et al. 1999). The two families of cloud trajectories arise from the difference in dynamics for different cloud column densities. The ratio of ram pressure and gravitational forces on a cloud is $F_{ram}/F_{grav} \sim N_{crit}/N_{H,c}$. Ram pressure is the stronger force when $N_{H,c} \lesssim N_{crit}$ while gravity dominates when $N_{H,c} \gtrsim N_{crit}$.

The analysis here mirrors the one in section 5.1 of Kartje et al. (1999) with minor differences. Assuming roughly spherical clouds, Kartje et al. introduced a nominal mass $M_{c,max}$ associated with radius R_c (their equation 24), which is related to N_{crit} via $M_{c,max} \sim N_{crit} R_c^2$. Then for a cloud with mass M_c and that radius, $F_{ram}/F_{grav} \sim M_{c,max}/M_c$. But the column of such a cloud is $N_{H,c} = M_c/\pi R_c^2$; thus, the results are the same since $M_{c,max}/M_c \sim N_{crit}/N_{H,c}$. The advantage of the current formulation is in demonstrating explicitly the complete separation between the properties of the wind (N_{crit}) and the cloud ($N_{H,c}$), and that the only relevant property of the cloud is its column density; neither mass nor size matters separately.

3.1.1 The critical column density

If \dot{M}_{acc} is the accretion rate into the BLR then a fraction γ is carried away by the wind while the fraction $1 - \gamma$ reaches the black hole, where it is converted to luminosity with the radiative efficiency η . That is, $\dot{M}_w = \gamma \dot{M}_{acc}$ and $L_{bol} = \eta(1 - \gamma)\dot{M}_{acc}c^2$ so that $L_{bol} = \eta(\gamma^{-1} - 1)\dot{M}_w c^2$. The fraction γ , obtained from considerations of angular momentum conservation for disc outflows, is ~ 0.1 – 0.25 (Emmering et al. 1992; Pelletier & Pudritz 1992). We adopt the single value $\gamma = 0.25$ so that $L_{bol} \approx 3\eta\dot{M}_w c^2$ and get from equations (3) and (1)

$$N_{crit}(R_d) \approx 4.3 \times 10^{22} \frac{1}{\eta_{-2}} \left(\frac{L_{45}}{M_7^{2/3}} \right)^{3/4} \text{ cm}^{-2}, \quad (6)$$

where $\eta_{-2} = \eta/0.01$. From this value on the BLR outer radius, N_{crit} increases inwards as $r^{-1/2}$ to a maximum of $\sim 10N_{crit}(R_d)$ on the BLR inner boundary. The behaviour of N_{crit} is dominated by the variation of $L_{bol}/M^{2/3}$, a quantity that spans more than 10 orders of magnitude across the combined set of AGN studied in Section 2.

3.2 Emission characteristics

The specific luminosity of a broad line can be written as $L_{BL}\phi(v)$, where L_{BL} is the overall line luminosity and $\phi(v)$ is the line profile as a function of velocity ($\int \phi dv = 1$). We discuss separately each component.

3.2.1 The ratio L_{BL}/L_{bol}

Two factors control L_{BL}/L_{bol} , the fraction of the AGN luminosity converted into emission in a particular line. The first is the fraction of continuum radiation intercepted by all clouds. It depends on the geometry of the BLR cloud distribution and on the cloud optical depths, and can be considered the BLR geometrical covering factor. The second is the efficiency with which an individual cloud reprocesses the absorbed continuum into emission in the particular line. Given a cloud density, column density and chemical composition, this reprocessing is determined by the continuum spectral shape and the magnitude of its local flux, $L_{bol}/4\pi r^2 \propto (R_d/r)^2$ (equation 1). All clouds with similar internal properties located at the same scaled radial distance r/R_d , i.e. same fraction of the BLR radial size, will produce the same line spectrum, whatever the luminosity. Therefore the line conversion fraction $C_{BL} = L_{BL}/L_{bol}$ does not contain any explicit dependence on luminosity; it depends only on the continuum spectral shape, the geometry of the cloud distribution and the internal properties of individual clouds.

3.2.2 Line profiles

The line profile $\phi(v)$ is determined by the kinematics and geometry of the cloud distribution. Detailed model calculations of broad-line profiles were reported for two different approaches. Emmering et al. (1992) analysed line emission from an ensemble of clouds moving along the streamlines of a hydromagnetic disc wind in an attempt to reproduce typical properties of observed AGN broad lines. One of the major challenges is the line shapes which show velocity widths in excess of $10\,000 \text{ km s}^{-1}$ together with central cusps with widths of only $\sim 300 \text{ km s}^{-1}$. Since such sharp cusps are seen in high-ionization permitted metal lines, e.g. C IV $\lambda 1549$, they cannot be solely attributed to the contribution of a narrow component. With suitable choice of parameters, Emmering et al. were able to reproduce the observed profile asymmetries and sharply cusped peaks when the emission was dominated by clouds at high altitudes; emission from low-altitude clouds tended to produce double-peaked profiles instead. Bottorff et al. (1997) performed similar calculations with some added details and applied them to the well-studied Seyfert 1 galaxy NGC 5548, successfully reproducing all observations including line profiles and reverberation measurements. Since these models employed clouds moving with the wind, they would be produced by the cloud equation of motion (equation 2) when the gravitational force is omitted. We denote the profiles produced from such motions $\phi^w(v)$.

The other approach, motivated by the double-peaked profiles observed in some AGN, invoked emission from the Keplerian accretion disc (Chen & Halpern 1989; Eracleous & Halpern 2003; Eracleous et al. 2009). These models successfully explain many details of double-peaked AGN observations and also show that the line profiles can turn into single-peaked shapes by the presence of a disc wind with suitable properties. Purely Keplerian trajectories would be produced by the cloud equation of motion (equation 2) when the ram pressure force is omitted. We denote the line profiles produced by such Keplerian motions $\phi^K(v)$.

3.2.3 Composite BLR emission

As shown in Section 3.1, clouds with subcritical columns, $N_{H,c} < N_{crit}$, move along the streamlines of disc winds, therefore, the profile of line emission from an ensemble of such clouds is $\phi^w(v)$. If the line conversion factor (the fraction of ionizing radiation which is

reprocessed and emitted by the BLR; Section 3.2.1) of the cloud distribution is C_{BL}^{W} , the specific line luminosity is $L_{\text{bol}} C_{\text{BL}}^{\text{W}} \phi^{\text{W}}(v)$. Similarly, the motions of supercritical clouds, $N_{\text{H,c}} > N_{\text{crit}}$, trace the disc Keplerian rotation, therefore, we can use $\phi^{\text{K}}(v)$ to describe the line profiles they generate. With a line conversion factor C_{BL}^{K} , the specific line luminosity for an ensemble of supercritical clouds is $L_{\text{bol}} C_{\text{BL}}^{\text{K}} \phi^{\text{K}}(v)$. As noted above, the fraction of the continuum converted to broad lines is smaller for low-lying trajectories than for the high-altitude wind trajectories, therefore, C_{BL}^{K} is significantly smaller than C_{BL}^{W} .

In the most general case, the BLR will contain a mix of both subcritical and supercritical clouds. Denote by f the fractional contribution of subcritical clouds to the overall line emission, then

$$\frac{L_{\text{BL}}}{L_{\text{bol}}} \phi(v) = f C_{\text{BL}}^{\text{W}} \phi^{\text{W}}(v) + (1 - f) C_{\text{BL}}^{\text{K}} \phi^{\text{K}}(v). \quad (7)$$

The mixture introduces a new fundamental element to broad-line emission. As discussed above, with a fixed continuum spectral shape, cloud distribution and individual cloud properties, both the profile ϕ and the line conversion fraction C_{BL} are independent of luminosity. But lowering the luminosity while keeping all other parameters fixed will lower the fraction f because N_{crit} decreases with L_{bol} (equation 6). Therefore every cloud with a given column $N_{\text{H,c}}$ becomes supercritical once L_{bol} has fallen below the value that yields $N_{\text{crit}} = N_{\text{H,c}}$. With clouds shifting from the sub- to supercritical category, the cloud distribution is changing even if all the underlying BLR properties such as individual cloud parameters, wind streamlines, etc., do not change. As a result, the observed line luminosity and profile (a combination of the elevated wind and low-disc components) are changing with L_{bol} .¹

3.2.4 Broad-line spectral evolution

Column densities of BLR clouds can be expected to cover a large range, but only those exceeding a minimal $N_{\text{H,min}} \sim 5 \times 10^{21} \text{ cm}^{-2}$ will contribute to the observed broad-line spectrum (e.g. Netzer 1990). An upper bound on $N_{\text{H,c}}$ can be deduced from time variability of X-ray observations, caused by the passage of obscuring clouds across the line of sight. Risaliti et al. (2002) find obscuring cloud columns in the range $\sim 10^{22} - 10^{23} \text{ cm}^{-2}$, although an exceptional case of a Compton thick cloud ($N_{\text{H,c}} > 10^{24} \text{ cm}^{-2}$) has also been recorded (Risaliti et al. 2007). Whatever the maximal column, it is reasonable to assume that clouds with lower columns are more abundant, namely, the cloud distribution rises towards lower $N_{\text{H,c}}$. When the column density of a cloud at distance r from the black hole is in the range

$$N_{\text{H,min}} \simeq 5 \times 10^{21} \text{ cm}^{-2} \lesssim N_{\text{H,c}} \lesssim N_{\text{crit}}(r), \quad (8)$$

the cloud is subcritical. The lower bound, $N_{\text{H,min}}$, is universal, set by atomic physics, while the upper bound, $N_{\text{crit}}(r)$, varies across the BLR as $r^{-1/2}$ (equation 3), in addition to its overall variation with the AGN luminosity and black hole mass (equation 6). A declining luminosity pushes the upper bound downward towards the lower one, shrinking the range of subcritical columns. As a result, clouds that were subcritical at the higher luminosity can become supercritical, their trajectories shifting away from the wind streamlines into the low-lying, rotating category (Fig. 9). This reduces the fraction f and shifts the BLR emission from the first term in equation (7)

to the second, lowering the broad-line strength and leading to the emergence of double-peaked profiles.

Shrinkage of the subcritical range with decreasing luminosity provides a natural explanation for the $1.0 \rightarrow 1.2/1.5 \rightarrow 1.8/1.9$ sequence as it continually increases the fraction of supercritical columns in the cloud population. The SL12 sample shows that in spite of the huge range of $L_{\text{bol}}/M^{2/3}$, observable changes in broad-line emission arise from relatively small variations in this variable: the separation between the mean values of the 1.0 and 1.5 sources in that sample is less than 40 per cent, with an additional decrease of just under 30 per cent separating the 1.8 from the 1.5 (Fig. 4). This behaviour indicates that the fractional contributions of sub- and supercritical clouds to the broad-line emission are roughly comparable in type 1 AGN. Indeed, the mean value of $L_{45}/M_{-7}^{2/3}$ for QSO and Seyfert 1 galaxies is 0.18 (see Fig. 2), and η is typically ~ 5 – 10 per cent in these sources (Martínez-Sansigre & Rawlings 2011). With $\eta_{-2} = 5$, the value of N_{crit} varies from $\sim 2 \times 10^{22} \text{ cm}^{-2}$ on the BLR inner boundary to a minimum of $2 \times 10^{21} \text{ cm}^{-2}$ on its outer edge. Since the distribution of cloud column densities can be expected to rise towards its lower end, subcritical columns can dominate the emission and lead to standard type 1 spectra, with supercritical columns still comprising a significant fraction. This explains why relatively small changes in $L_{\text{bol}}/M^{2/3}$ from its particular value in type 1 AGN suffice to tip the balance between the two families of trajectories, triggering the change in spectral type.

At the lower luminosities of the EH09 sample, supercritical columns dominate decisively. In type 1.8/1.9 sources, the histograms in Fig. 2 show that the mean value of $L_{\text{bol}}/M^{2/3}$ is three orders of magnitudes lower than for type 1.0. If η were the same for both classes, N_{crit} for type 1.8/1.9 would be only $\sim 1 \times 10^{20} \text{ cm}^{-2}$ on the BLR inner boundary and all clouds would be supercritical everywhere. However, in all likelihood the accretion in these sources has a low radiative efficiency, with $\eta \lesssim 10^{-3}$ (see Ho 2008 and references therein), so N_{crit} can be expected to be comparable to $N_{\text{H,min}}$ on the inner boundary (equation 6). This would still make the cloud population of type 1.8/1.9 dominated by supercritical column densities, resulting in weaker broad-line emission together with double-peaked profiles when viewed from suitable angles. Further decrease of the accretion rate triggers the mass conservation limit found in EH09, broad-line emission disappears and the AGN becomes a true type 2.

4 SUMMARY AND DISCUSSION

Intermediate-type AGN have been generally dismissed as a minor detail of unification. Instead, the data now show that as the accretion rate decreases, broad-line emission progressively declines from its high intensity in quasars and Seyfert 1 galaxies to the lower relative strength of intermediate-type AGN, disappearing altogether at sufficiently low luminosities. As summarized in Fig. 8, a decreasing accretion rate is accompanied by a decrease in the fraction of bolometric luminosity converted into broad-line emission. This systematic behaviour is at odds with the fine-tuning required by explanations of the intermediate types that were based on partial obscuration or transient radiative transfer effects (e.g. Korista & Goad 2004). It also cannot be explained by a change in the continuum spectral shape. Although the disappearance of the big blue bump causes significant variation of the spectral energy distribution from high- to low-luminosity AGN (see e.g. Ho 2008, fig. 7), an explanation based on such changes could not apply to the SL12 data set. Thanks to a sizeable number of sources, this sample provides decisive evidence for transitions to intermediate spectral classes at

¹ Integrating equation (7) over v yields $C_{\text{BL}} = f C_{\text{BL}}^{\text{W}} + (1 - f) C_{\text{BL}}^{\text{K}}$, and the overall profile is $\phi(v) = (C_{\text{BL}}^{\text{W}}/C_{\text{BL}}) f \phi^{\text{W}}(v) + (C_{\text{BL}}^{\text{K}}/C_{\text{BL}}) (1 - f) \phi^{\text{K}}(v)$.

fairly high luminosities – the mean luminosity is $3 \times 10^{44} \text{ erg s}^{-1}$ for the sample type 1.0 objects, $1 \times 10^{44} \text{ erg s}^{-1}$ for the 1.5 and $4 \times 10^{43} \text{ erg s}^{-1}$ for the 1.8. There are no significant changes in continuum spectral shape among such luminosities; indeed, such changes do not show up across the entire SL12 data set, whose luminosity range is $L_{\text{bol}} = 3 \times 10^{42} - 2 \times 10^{46} \text{ erg s}^{-1}$ (Stern & Laor 2012a). The spectral sequence $1 \rightarrow 1.2/1.5 \rightarrow 1.8/1.9 \rightarrow 2$ is a true evolutionary sequence, reflecting evolution of the BLR structure with decreasing accretion rate on to the central black hole. The emergence of double-peaked profiles along the sequence is additional support for such an inherent structural change.

According to standard unification, the torus obscuration and the observer location are the only factors in determining the spectral class of any given AGN. There is no a priori expectation for the broad-line spectrum to correlate with $L_{\text{bol}}/M^{2/3}$. Yet the spectral classes of broad-line emitters cluster around different values of $L_{\text{bol}}/M^{2/3}$ and this variable controls the evolutionary sequence of type $1 \rightarrow 1.2/1.5 \rightarrow 1.8/1.9 \rightarrow 2$. Additionally, double-peaked profiles emerge along this sequence. Both trends find a natural explanation in the disc-wind scenario for the BLR: as the luminosity decreases, more and more clouds shift from high-altitude trajectories along the wind streamlines to low-altitude motion that follows closely the disc rotation (Fig. 9). This reduces the fraction of the continuum intercepted by the BLR – hence the reduction in line strengths – and leads to the emergence of double-peaked emission. The transition between the two families of trajectories is controlled by a wind-determined critical column N_{crit} (equations 3 and 6); this accounts for the $L_{\text{bol}}/M^{2/3}$ dependence. This transition happens even if neither cloud properties nor wind structure change with luminosity. It occurs under a broad range of conditions, as it arises simply from the competition between the black hole gravity and the wind ram pressure, irrespective of the detailed mechanisms that drive and control the outflow. Furthermore, this mechanism properly explains the values of $L_{\text{bol}}/M^{2/3}$ at the transitions from one spectral class to the next in spite of the huge variation range of this variable that spans more than 10 orders of magnitude. The quantity that sets the scale for these transitions is $N_{\text{H, min}} \sim 5 \times 10^{21} \text{ cm}^{-2}$, the minimal column density for clouds to partake in broad-line emission. $N_{\text{H, min}}$ is determined purely by atomic constants, entirely independent of any considerations that involve the BLR detailed structure. This fundamental quantity sets the proper scale for the transitions between spectral classes without any free parameters or fine tuning, another success of the disc-wind scenario.

It is important to note that exceptions exist: not every double-peaked object has a low Eddington ratio and not every intermediate-type AGN has a low luminosity. Such cases are to be expected since the BLR structure is anything but simple. Still, the trends are quite clear and fit well into the outflow scenario. While the variable $L_{\text{bol}}/M^{2/3}$, which is close to the Eddington ratio, emerges naturally, it controls only one aspect of the disc outflow; other dynamical effects may introduce additional dependencies. For example, Nicastro (2000) considered the interplay between radiation pressure and gas pressure on the outflow and found a dependence on $L_{\text{bol}}/M^{7/8}$, practically indistinguishable from $L_{\text{bol}}/M^{2/3}$. Similarly, the growing importance of radiatively inefficient accretion flows at lower Eddington ratios could also play a role in the BLR evolution, especially in governing the details of the transition between various spectral classes (Ho 2008; Trump et al. 2011). Moreover, while the bulk of the data shows diminishing broad-line emission with accretion rate, two recent discoveries buck the trend. Ho, Kim & Terashima (2012) and Miniutti et al. (2013) have found AGN with very low black hole masses ($10^5 - 10^6 M_{\odot}$) and very high Eddington

ratios, but no broad lines. In both cases, the absence of broad lines is highly significant. Because of their high Eddington ratios, both objects are above the EH09 boundary (Fig. 1), an absolute limit that follows from mass conservation. This limit implies that there should be only true type 2 objects below the EH09 boundary, but it does not preclude true type 2 AGN above it. Still, these objects do not fit the general observed pattern and are not explained by our scenario. They require another explanation, and some possibilities are discussed in Miniutti et al. (2013).

Model calculations employing clouds moving along disc-wind streamlines successfully explain details of broad-line profiles, including their difficult-to-explain sharply cusped peaks (Emmering et al. 1992). Model calculations of disc emission successfully explain the double-peaked profiles observed in some AGN (Eracleous et al. 2009). The first class of models corresponds to $f=1$ in equation (7), the second to $f=0$; therefore, our model accrues all the benefits of both earlier models at the two proper ends of the accretion rate spectrum. A full calculation of the combined profiles and line strengths with accretion rate is a complex task. Other broad emission lines may also deviate slightly from the behaviour observed for H α since the supercritical clouds may receive insufficient ionizing flux to support the higher ionization broad lines (e.g. Proga, Stone & Kallman 2000; Proga & Kallman 2004). This arises from the combined effect of a decrease of the ionization parameter at low altitudes because of the continuum anisotropy and the change in the ionizing continuum spectral shape at low luminosities. We plan on performing such detailed calculations and will report their results in future publications.

4.1 Observational challenges

Observations of intermediate-type AGN present unique challenges. Based on line spectra alone, NGC 1068 would be classified as type 1.8, NGC 4388 as 1.9. Yet both are Seyfert 2 galaxies with obscured nuclei (Compton-thick obscuration in the case of NGC 1068) whose weak broad lines reflect scattered light, as determined by polarization measurements (Antonucci & Miller 1985; Young et al. 1996). In an inherent ambiguity, type 1.8/1.9 spectra can arise from either the directly arriving weak broad-line emission of an unobscured nucleus, intrinsically a type 1.8/1.9 AGN, or indirectly through the scattering of strong broad lines from an obscured nucleus. The latter is an obscured type 2 AGN appearing as a spurious 1.8/1.9 object because of a hidden central engine whose intrinsic broad-line strength is that of a type 1 source. Spectral information alone is insufficient to resolve the ambiguity of these two very different situations. A decisive determination of the true nature of a type 1.8/1.9 spectrum requires also a measurement of the obscuration to the nucleus, ideally supplemented by a measurement of the broad-line polarization.

Since N_{crit} varies as $r^{-1/2}$ (equation 3), the transition from high-altitude wind trajectories to low-altitude disc-like rotation when L_{bol} is decreasing should occur first at larger radii. Lines emitted further out in the BLR should thus be the first to display reduced relative strengths and double-peaked emission profiles at lower luminosities. This provides a testable prediction of the mechanism proposed here.

Much of the support for the data analysis presented here comes from the SL12 sample, which was culled out of the SDSS data base. For the most part, these observations lacked the angular resolution to separate the AGN from the host galaxy and could not identify AGN with luminosities below $\sim 10^{42} \text{ erg s}^{-1}$, where the bulk of the intermediate-type population is expected. But what the SL12 sample lacked in luminosity coverage it made up in sheer size, showing the power of large samples to reliably identify trends in

the data. As can be seen from Fig. 1, the crucial low-luminosity end where most intermediate-type AGN can be expected to reside and most of the BLR evolution to occur is covered only sparsely in comparison. Future observations with higher angular resolution are needed to fill this gap and provide more complete coverage of the full evolution of the AGN BLR.

ACKNOWLEDGEMENTS

We thank Jonathan Stern and Lisa Winter for providing us with their data. Special thanks to Ari Laor and Jonathan Stern for their help and useful comments, and to Jorge Pineda for help with the KS test. ME acknowledges the award of an NPP Senior Fellowship from ORAU, which supported a sabbatical leave at JPL/Caltech where much of this work was completed. The work of LCH is supported by the Kavli Foundation, Peking University, the Chinese Academy of Sciences and Carnegie Institution for Science. JRT is supported by NASA through Hubble Fellowship grant HST-HF-51330.01 awarded by the Space Telescope Science Institute, which is operated by the Association of Universities for Research in Astronomy, Inc., for NASA, under contract NAS 5-26555.

REFERENCES

- Antonucci R., 1993, *ARA&A*, 31, 473
- Antonucci R. R. J., Miller J. S., 1985, *ApJ*, 297, 621
- Blandford R. D., Payne D. G., 1982, *MNRAS*, 199, 883
- Bottorff M., Korista K. T., Shlosman I., Blandford R. D., 1997, *ApJ*, 479, 200
- Bottorff M. C., Korista K. T., Shlosman I., 2000, *ApJ*, 537, 134
- Chen K., Halpern J. P., 1989, *ApJ*, 344, 115
- Elitzur M., 2008, *New Astron. Rev.*, 52, 274
- Elitzur M., Ho L. C., 2009, *ApJ*, 701, L91 (EH09)
- Elitzur M., Shlosman I., 2006, *ApJ*, 648, L101
- Emmering R. T., Blandford R. D., Shlosman I., 1992, *ApJ*, 385, 460
- Eracleous M., Halpern J. P., 2003, *ApJ*, 599, 886
- Eracleous M., Lewis K. T., Flohic H. M. L. G., 2009, *New Astron. Rev.*, 53, 133
- Everett J. E., 2005, *ApJ*, 631, 689
- Everett J. E., 2007, *Ap&SS*, 311, 269
- Ferrarese L., Merritt D., 2000, *ApJ*, 539, L9
- Fukumura K., Kazanas D., Contopoulos I., Behar E., 2010, *ApJ*, 723, L228
- Gebhardt K. et al., 2000, *ApJ*, 539, L13
- Greene J. E., Ho L. C., 2007, *ApJ*, 667, 131 (GH07)
- Greene J. E., Ho L. C., Ulvestad J. S., 2006, *ApJ*, 636, 56
- Hall P. B., Hutsemekers D., Anderson S. F., Brinkmann J., Fan X., Schneider D. P., York D. G., 2003, *ApJ*, 593, 189
- Hall P. B., Sadavoy S. I., Hutsemekers D., Everett J. E., Rafiee A., 2007, *ApJ*, 665, 174
- Ho L. C., 2008, *ARA&A*, 46, 475
- Ho L. C., 2009, *ApJ*, 699, 626
- Ho L. C., Filippenko A. V., Sargent W. L. W., 1997, *ApJS*, 112, 315
- Ho L. C., Rudnick G., Rix H.-W., Shields J. C., McIntosh D. H., Filippenko A. V., Sargent W. L. W., Eracleous M., 2000, *ApJ*, 541, 120
- Ho L. C., Filippenko A. V., Sargent W. L. W., 2003, *ApJ*, 583, 159
- Ho L. C., Kim M., Terashima Y., 2012, *ApJ*, 759, L16
- Kartje J. F., Königl A., 1996, *Vistas Astron.*, 40, 133
- Kartje J. F., Königl A., Elitzur M., 1999, *ApJ*, 513, 180
- Kawaguchi T., Mori M., 2010, *ApJ*, 724, L183
- Kollatschny W., 2003, *A&A*, 407, 461
- Kollatschny W., Zetzl M., 2013, *A&A*, 551, L6
- Königl A., Kartje J. F., 1994, *ApJ*, 434, 446
- Korista K. T., Goad M. R., 2004, *ApJ*, 606, 749
- Kormendy J., Ho L. C., 2013, *ARA&A*, 51, 511
- Laor A., 2003, *ApJ*, 590, 86
- Laor A., Netzer H., 1989, *MNRAS*, 238, 897
- Mann H. B., Whitney D. R., 1947, *Ann. Math. Stat.*, 18, 50
- Maoz D., Nagar N. M., Falcke H., Wilson A. S., 2005, *ApJ*, 625, 699
- Marconi A., Hunt L. K., 2003, *ApJ*, 589, L21
- Marconi A., Risaliti G., Gilli R., Hunt L. K., Maiolino R., Salvati M., 2004, *MNRAS*, 351, 169
- Martínez-Sansigre A., Rawlings S., 2011, *MNRAS*, 418, L84
- Miniutti G., Saxton R. D., Rodríguez-Pascual P. M., Read A. M., Esquej P., Colless M., Dobbie P., Spolaor M., 2013, *MNRAS*, 433, 1764
- Neškova M., Sirocky M. M., Nikutta R., Ivezić Z., Elitzur M., 2008, *ApJ*, 685, 160
- Netzer H., 1990, in Courvoisier T. J. L., Mayor M., eds, *Active Galactic Nuclei*. Springer-Verlag, Berlin, p. 57
- Nicastro F., 2000, *ApJ*, 530, L65
- Osterbrock D. E., 1981, *ApJ*, 249, 462
- Panessa F., Bassani L., 2002, *A&A*, 394, 435
- Pelletier G., Pudritz R. E., 1992, *ApJ*, 394, 117
- Peterson B. M., 2006, in Alloin D., ed., *Lecture Notes in Physics*, Vol. 693, *Physics of Active Galactic Nuclei at All Scales*. Springer-Verlag, Berlin, p. 77
- Proga D., 2007, in Ho L. C., Wang J.-W., eds, *ASP Conf. Ser. Vol. 373, The Central Engine of Active Galactic Nuclei*. Astron. Soc. Pac., San Francisco, p. 267
- Proga D., Kallman T. R., 2004, *ApJ*, 616, 688
- Proga D., Stone J. M., Kallman T. R., 2000, *ApJ*, 543, 686
- Rees M. J., 1987, *MNRAS*, 228, 47P
- Richards G. T. et al., 2011, *AJ*, 141, 167
- Risaliti G., Elvis M., Nicastro F., 2002, *ApJ*, 571, 234
- Risaliti G., Elvis M., Fabbiano G., Baldi A., Zezas A., Salvati M., 2007, *ApJ*, 659, L111
- Risaliti G., Salvati M., Marconi A., 2011, *MNRAS*, 411, 2223
- Runnoe J. C., Brotherton M. S., Shang Z., 2012, *MNRAS*, 422, 478
- Schurch N. J., Done C., Proga D., 2009, *ApJ*, 694, 1
- Scoville N. et al., 2007, *ApJS*, 172, 1
- Shields J. C., Rix H.-W., McIntosh D. H., Ho L. C., Rudnick G., Filippenko A. V., Sargent W. L. W., Sarzi M., 2000, *ApJ*, 534, L27
- Slone O., Netzer H., 2012, *MNRAS*, 426, 656
- Soltan A., 1982, *MNRAS*, 200, 115
- Stern J., Laor A., 2012a, *MNRAS*, 423, 600
- Stern J., Laor A., 2012b, *MNRAS*, 426, 2703
- Strateva I. V. et al., 2003, *AJ*, 126, 1720
- Sun W.-H., Malkan M. A., 1989, *ApJ*, 346, 68
- Tran H. D., 2001, *ApJ*, 554, L19
- Tran H. D., 2003, *ApJ*, 583, 632
- Tremaine S. et al., 2002, *ApJ*, 574, 740
- Trippe M. L., Crenshaw D. M., Deo R. P., Dietrich M., Kraemer S. B., Rafter S. E., Turner T. J., 2010, *ApJ*, 725, 1749
- Trump J. R. et al., 2011, *ApJ*, 733, 60
- van der Wolk G., Barthel P. D., Peletier R. F., Pel J. W., 2010, *A&A*, 511, A64
- Winter L. M., Veilleux S., McKernan B., Kallman T. R., 2012, *ApJ*, 745, 107 (W12)
- Young S., Hough J. H., Efstathiou A., Wills B. J., Bailey J. A., Ward M. J., Axon D. J., 1996, *MNRAS*, 281, 1206

This paper has been typeset from a \LaTeX file prepared by the author.